2024 IEEE/RSJ International Conference on Intelligent Robots and Systems (IROS)
October 14-18, 2024. Abu Dhabi, UAE

A Unified Framework of Hybrid Vision-Force Control With Nullspace Compliance for Redundant Robots

Zhiwen Li[2], Weibing Li[2], Yanjie Chen[3], and Yongping Pan[1]

***Abstract*— The ability to handle contact makes robots qualified for many complicated tasks, such as welding, hammering, and wiping. Robot cameras facilitate position planning and control without the geometric knowledge of contact surfaces since they can project contact surfaces onto a 2-dimensional image plane. However, existing hybrid vision-force control (HVFC) methods still rely on this knowledge to project the force on the constraint subspace and do not adequately leverage the redundant degrees of freedom (DoFs) for redundant robots with contact tasks. This paper proposes an enhanced HVFC solution for redundant robots equipped with an eye-to-hand camera to unify HVFC in the Cartesian space and impedance control in the joint nullspace into one closed-loop dynamics with rigorous stability guarantees. Any geometric knowledge of contact surfaces is not required by projecting the force into the redundant space of the visual task rather than the surface's normal space. Experiments on a seven-DoF collaborative robot have verified that the proposed method is qualified for simultaneous contact tasks in the Cartesian space and compliant interaction in the joint nullspace.**

I. Introduction

Contact between robot tooltips and environments frequently occurs during complex operations, flexible object manipulation, and interactions [1]. The ability to handle robot-environment contact becomes crucial for versatile robots to assist humans with repetitive, tedious, and time-consuming tasks in factories, such as spot-welding, deburring, and assembly [2]. Hybrid position-force control has been widely studied to tackle robotic applications with surface contact, e.g., see [3]–[8], where the essential idea is to control position and force in two separative subspaces [9]. But many of the existing methods rely on the geometric knowledge of the surface [3], [4]. Although some of them get rid of this dependency [5]–[8], challenges remain with aspect to computational efficiency, rigorous stability analysis [5], the complex mechanical structure of macro-micro robots [8], and a stringent condition of persistent excitation for the accuracy estimation of the surface normal [6], [7]. Moreover, as the desired signal of the above methods is the Cartesian coordinate of the contact point, surface-based position planning requires the extra processes of offline teaching without the surface geometry, degrading their practicability for real-time operations and teleoperations.

Cameras (i.e., vision sensors) can project 3-dimensional objects onto a 2-dimensional image plane. Thereby, position planning and control can be directly operated on the image plane through image-based visual servoing without any prior geometric knowledge of the surface. Besides, cameras facilitate teleoperation, enabling robots to work in tough and dangerous environments. Therefore, hybrid vision-force control (HVFC), as a natural evolution of hybrid position-force control, has attracted much attention, where the vision feedback from a monocular camera with the eye-in-hand [10], [11] or eye-to-hand (ETH) [12]–[15] configuration can be applied to control the position on the surface for various robots, e.g., unmanned aerial manipulators [10], rigid robot manipulators [11]–[14], and soft robots [15]. Regarding the HVFC methods for rigid robot manipulators, there exist several limitations: 1) The exact surface geometric knowledge is required in [12]; 2) an approximate surface normal instead of the exact one is used in [14]; 3) the tooltip orientation or contact force is assumed to be along the surface normal, which are then used to estimate the surface normal in [11], [13]; 4) none of them fully exploit the redundant property of multi-DoF robot manipulators.

Motivated by the above investigation, this paper presents a novel HVFC framework for redundant robot manipulators with a monocular ETH camera to perform contact tasks on rigid surfaces. Specifically, two translational degrees of freedom (DoFs) of the tooltip are allocated for precise position control on contact surfaces, while an additional DoF is dedicated to force control so that it does not require any prior geometric knowledge or the extra model estimation of contact surfaces. The desired target is expressed in image coordinates, which eliminates the need for geometric knowledge in position planning. Moreover, the remaining DoFs are effectively employed for nullspace impedance control to ensure safe interactions to some extent by sufficiently exploiting the redundancy of multi-DoF robot manipulators. Hence, the proposed method unifies visual servoing, force control, and impedance control in a stable closed-loop system, which distinguishes it from existing HVFC methods. Experiments are conducted on a seven-DoF collaborative robot to validate the qualification of the proposed HVFC for contact tasks on rigid surfaces and compliant interactions in the joint nullspace.

Notation: $\mathbb{R}$, $\mathbb{R}^+$, $\mathbb{R}^n$, and $\mathbb{R}^{m\times n}$ represent the spaces of real numbers, positive real numbers, real n-vectors, and real $m \times n$-matrices, respectively, $\mathbb{N}$ denotes the set of natural numbers, $\mathbf{0}$ denotes a zero matrix or vector, $\max\{\cdot\}$ denotes the maximum operator, $\|\boldsymbol{x}\|$ denotes the Euclidean norm of

*This work was supported in part by the Fundamental Research Funds for the Central Universities, Sun Yat-sen University, China, under Grant 23lgzy004 and in part by the National Natural Science Foundation of China under Grant 62273098 (*Corresponding author: Yongping Pan*).

[1]Yongping Pan is with the School of Advanced Manufacturing, Sun Yat-sen University, Shenzhen 518100, China panyongp@mail.sysu.edu.cn

[2]Zhiwen Li and Weibing Li are with the School of Computer Science and Engineering, Sun Yat-sen University, Guangzhou 510006, China lizhw63@mail3.sysu.edu.cn, liwb53@mail.sysu.edu.cn

[3]Yanjie Chen is with the School of Mechanical Engineering and Automation, Fuzhou University, Fuzhou 350108, China chenyanjiehnu@gmail.com

$\boldsymbol{x}$, diag$(x_1, x_2, \cdots, x_n)$ is a diagonal matrix with diagonal elements x_i to x_n, and rank(B) is the rank of B, where n, $m \in \mathbb{N}$, $\boldsymbol{x} \in \mathbb{R}^n$, $x_i \in \mathbb{R}$, $A_i \in \mathbb{R}^{m\times n}$, and $B \in \mathbb{R}^{m\times n}$.

II. Camera Projection Model

Consider a redundant robotic system in Fig. 1 where an ETH camera is fixed on the world frame $\{B\}$, and a feature point Q is rigidly attached to the robot end-effector. Without loss of generality, we assume that Q is the tooltip. Then, the projection model of a pin-hole camera is built in this section.

Let $\boldsymbol{x}(t) \in \mathbb{R}^3$ denote the coordinate of Q in $\{B\}$, $\boldsymbol{p}(t) = [u, v, 1]^T \in \mathbb{R}^3$ be its homogeneous pixel coordinate on the image plane, $u(t), v(t) \in \mathbb{R}$ be the coordinates at the u and v-axes, respectively, $K \in \mathbb{R}^{3\times3}$ be an intrinsic camera parameter, and ${}^cT_\mathrm{b} \in \mathbb{R}^{3\times4}$ be an extrinsic camera parameter given by

$$ {}^cT_\mathrm{b} = \begin{bmatrix} {}^cR_\mathrm{b} & {}^c\boldsymbol{t}_\mathrm{b} \end{bmatrix} \tag{1} $$

with ${}^cR_\mathrm{b} \in \mathbb{R}^{3\times3}$ and ${}^c\boldsymbol{t}_\mathrm{b} \in \mathbb{R}^3$ denoting the rotation matrix and the translation vector from the world frame $\{B\}$ to the camera frame $\{C\}$, respectively. Then, the projection model of a pinhole camera can be represented by [16]

$$ \boldsymbol{p} = \frac{1}{z}(R\boldsymbol{x} + \boldsymbol{t}) \tag{2} $$

in which $R := K{}^cR_\mathrm{b} \in \mathbb{R}^{3\times3}$ and $\boldsymbol{t} := K{}^c\boldsymbol{t}_b \in \mathbb{R}^3$ are two constant parameters of the ETH camera, and $z(t) \in \mathbb{R}^+$ is the depth of Q in $\{C\}$ calculated by

$$ z(t) = \boldsymbol{r}_3^T\boldsymbol{x} + t_3 \tag{3} $$

in which $\boldsymbol{r}_3^T \in \mathbb{R}^3$ is the 3rd row of R, and $t_3 \in \mathbb{R}$ is the 3rd element of $\boldsymbol{t}$. Taking the time derivation of (2) and (3), one gets the following velocity relationships:

$$ \dot{\boldsymbol{p}}(t) = \frac{1}{z}A\dot{\boldsymbol{x}} \in \mathbb{R}^3, \tag{4} $$

$$ \dot{z}(t) = \boldsymbol{r}_3^T\dot{\boldsymbol{x}} \in \mathbb{R} \tag{5} $$

where $A(t) := R - \boldsymbol{p}\boldsymbol{r}_3^T \in \mathbb{R}^{3\times3}$ is an depth-independent image Jacobian matrix .

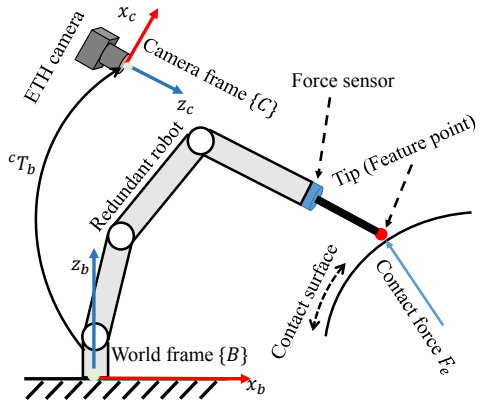

Fig. 1. An illustration of a redundant robot with vision and force feedback, where the robot has more DoFs than tasks in the Cartesian space.

III. A Unified Control Framework

In the redundant robotic system shown in Fig. 1, the position $\boldsymbol{x}$ of the tooltip (i.e., Q) is observed by an ETH camera, and a force sensor mounted on the wrist is used to measure the contact force $F_\mathrm{e} \in \mathbb{R}^3$. Fig. 2 shows the block diagram of the overall system, where impedance control is implemented in the joint nullspace to fully use robot redundancy, and an HVFC method is developed in the Cartesian space to perform surface contact tasks with 3 DoFs.

A. Joint Nullspace Impedance Control

The dynamics of an n-DoF redundant robotic manipulator can be described by an Euler-Lagrange formulation

$$ M(\boldsymbol{q})\ddot{\boldsymbol{q}} + C(\boldsymbol{q}, \dot{\boldsymbol{q}})\dot{\boldsymbol{q}} + \boldsymbol{g}(\boldsymbol{q}) = \boldsymbol{\tau}_\mathrm{c} + \boldsymbol{\tau}_\mathrm{e} \tag{6} $$

where $\boldsymbol{q}(t)$, $\dot{\boldsymbol{q}}(t)$ and $\ddot{\boldsymbol{q}}(t) \in \mathbb{R}^n$ are vectors of joint positions, velocities, and accelerations, respectively, $M(\boldsymbol{q}) \in \mathbb{R}^{n\times n}$ is an inertial matrix, $C(\boldsymbol{q}, \dot{\boldsymbol{q}}) \in \mathbb{R}^{n\times n}$ is a centripetal-Coriolis matrix, and $\boldsymbol{g}(\boldsymbol{q})$, $\boldsymbol{\tau}_\mathrm{c}(t)$, $\boldsymbol{\tau}_\mathrm{e}(t) \in \mathbb{R}^n$ are vectors of gravity, control, and external torques, respectively. Note that $\boldsymbol{\tau}_\mathrm{e}$ can be measured by torque sensors or estimated as in [17]. The velocity $\dot{\boldsymbol{x}} \in \mathbb{R}^3$ and acceleration $\ddot{\boldsymbol{x}} \in \mathbb{R}^3$ of the feature point Q in the Cartesian space are generated by

$$ \dot{\boldsymbol{x}} = J(\boldsymbol{q})\dot{\boldsymbol{q}}, \ \ddot{\boldsymbol{x}} = J(\boldsymbol{q})\ddot{\boldsymbol{q}} + \dot{J}(\boldsymbol{q})\dot{\boldsymbol{q}} \tag{7} $$

where $J(\boldsymbol{q}) \in \mathbb{R}^{3\times n}$ is the translational part of a robot Jacobian of Q. As only the nonsingular case is considered here, one has rank$(J(\boldsymbol{q})) = 3$. Let the nullspace projection matrix be $N := I - J^NJ \in \mathbb{R}^{n\times n}$ with $J^N := M^{-1}J^T(JM^{-1}J^T)^{-1} \in \mathbb{R}^{n\times n}$ [18]. Then, N has the following properties: 1) $JN = \mathbf{0}$; 2) $NM^{-1}J^T = \mathbf{0}$; 3) $NN = N$; 4) $MN = N^TM$ [19].

Applying an overall control torque

$$ \boldsymbol{\tau}_\mathrm{c} = J^T(\boldsymbol{q})F_\mathrm{c} + MN\boldsymbol{\tau}_\mathrm{n} + C(\boldsymbol{q}, \dot{\boldsymbol{q}})\dot{\boldsymbol{q}} + \boldsymbol{g}(\boldsymbol{q}) \tag{8} $$

to (6) with $F_\mathrm{c} \in \mathbb{R}^3$ and $\boldsymbol{\tau}_\mathrm{n} \in \mathbb{R}^n$ being the input forces in the Cartesian space and joint nullspace, respectively, one gets

$$ \ddot{\boldsymbol{q}} = M^{-1}J^TF_\mathrm{c} + N\boldsymbol{\tau}_\mathrm{n} + M^{-1}\boldsymbol{\tau}_\mathrm{e}. \tag{9} $$

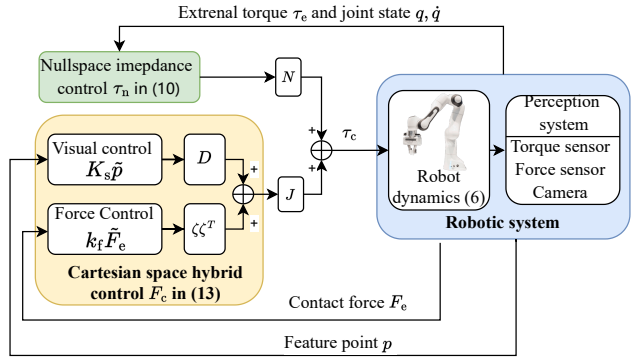

Fig. 2. A block diagram of the proposed HVFC framework. Note that this framework does not depend on any geometric knowledge of the contact surface, and the control torque $\boldsymbol{\tau}_\mathrm{c}$ and the hybrid control force F_c also include other items that are used for nonlinear compensation.

Design a control torque $\boldsymbol{\tau}_{\mathrm{n}}$ in the joint nullspace

$$\boldsymbol{\tau}_{\mathrm{n}} = \ddot{\boldsymbol{q}}_{\mathrm{d}} - M_{\mathrm{d}}^{-1}(B_{\mathrm{d}}\dot{\tilde{\boldsymbol{q}}} + K_{\mathrm{d}}\tilde{\boldsymbol{q}}), \tag{10}$$

where $\tilde{\boldsymbol{q}}(t) := \boldsymbol{q}_{\mathrm{d}}(t) - \boldsymbol{q}(t) \in \mathbb{R}^n$ is a tracking error with $\boldsymbol{q}_{\mathrm{d}}(t) \in \mathbb{R}^n$ being the desired joint position, and M_{d}, B_{d}, and $K_{\mathrm{d}} \in \mathbb{R}^{n\times n}$ are the positive-definite desired inertia, damping, and stiffness matrices, respectively.

B. Cartesian Space Hybrid Control

Let $\tilde{\boldsymbol{p}} := \boldsymbol{p} - \boldsymbol{p}_{\mathrm{d}} \in \mathbb{R}^3$ be a pixel error and $\tilde{F}_{\mathrm{e}} := F_{\mathrm{e}} - F_{\mathrm{d}} \in \mathbb{R}^3$ be a contact force error, where $\boldsymbol{p}_{\mathrm{d}} \in \mathbb{R}^3$ and $F_{\mathrm{d}} \in \mathbb{R}^3$ are the desired pixel position and the desired contact force, respectively. Then, the objective is expressed by

$$\tilde{\boldsymbol{p}} \to \mathbf{0},\ \tilde{F}_{\mathrm{e}} \to \mathbf{0}.$$

First, left-multiplying both sides of (9) by J and using the property $JN = \mathbf{0}$, one obtains

$$J\ddot{\boldsymbol{q}} = JM^{-1}J^T F_{\mathrm{c}} + JM^{-1}\boldsymbol{\tau}_{\mathrm{e}}. \tag{11}$$

Then, combining (11) with (7) leads to

$$\Lambda\ddot{\boldsymbol{x}} - \Lambda\dot{J}(\boldsymbol{q})\dot{\boldsymbol{q}} = F_{\mathrm{c}} + \Lambda JM^{-1}\boldsymbol{\tau}_{\mathrm{e}} \tag{12}$$

with $\Lambda := (JM^{-1}J^T)^{-1} \in \mathbb{R}^{3\times3}$. Before giving the hybrid control force F_{c}, we present the following property.

Property 1: Let $D := A^T + \frac{1}{2}\boldsymbol{r}_3\tilde{\boldsymbol{p}}^T \in \mathbb{R}^{3\times3}$ and $Z := [\boldsymbol{d}_1, \boldsymbol{d}_2, \boldsymbol{r}_3] \in \mathbb{R}^{3\times3}$ with $\boldsymbol{d}_i \in \mathbb{R}^3$ being the ith column of D. If rank(R) = 3, one has rank(D) = 2 and rank(Z) = 3. Besides, denoting $\boldsymbol{\zeta}^T \in \mathbb{R}^3$ as a normalized vector of the 3rd row of Z^{-1}, one has $\boldsymbol{\zeta}^T\boldsymbol{\zeta} = 1$, $\boldsymbol{\zeta}^T D = \mathbf{0}$, and $D^T\boldsymbol{\zeta} = \mathbf{0}$.

Proof: 1) Using the definition of A in (4), one gets

$$\begin{aligned} D &= A^T + \frac{1}{2}\boldsymbol{r}_3\tilde{\boldsymbol{p}}^T = R^T - \boldsymbol{r}_3\boldsymbol{p}^T + \frac{1}{2}\boldsymbol{r}_3\tilde{\boldsymbol{p}}^T \\ &= R^T - \frac{1}{2}\boldsymbol{r}_3(\boldsymbol{p} + \boldsymbol{p}_{\mathrm{d}})^T = \left(R^T - \boldsymbol{r}_3\boldsymbol{\eta}^T\right) \end{aligned}$$

with $\boldsymbol{\eta} = [\eta_1, \eta_2, \eta_3]^T := \frac{1}{2}(\boldsymbol{p} + \boldsymbol{p}_{\mathrm{d}}) \in \mathbb{R}^3$ and $\eta_3 = 1$, so

$$\begin{aligned} D &= \begin{bmatrix} \boldsymbol{r}_1 - \eta_1\boldsymbol{r}_3 & \boldsymbol{r}_2 - \eta_2\boldsymbol{r}_3 & 0 \end{bmatrix}, \\ Zn &= \begin{bmatrix} \boldsymbol{r}_1 - \eta_1\boldsymbol{r}_3 & \boldsymbol{r}_2 - \eta_2\boldsymbol{r}_3 & \boldsymbol{r}_3 \end{bmatrix}. \end{aligned}$$

If rank(D) < 2, there must exist two real numbers $k_1, k_2 \in \mathbb{R}$ that are not all 0, such that $k_1(\boldsymbol{r}_1 - \eta_1\boldsymbol{r}_3) + k_2(\boldsymbol{r}_2 - \eta_2\boldsymbol{r}_3) = 0$ that can be rearranged to $k_1\boldsymbol{r}_1 + k_2\boldsymbol{r}_2 + (-k_1\eta_1 - k_2\eta_2)\boldsymbol{r}_3 = 0$. As this equation collides with rank(R) = 3 even when $-k_1\eta_1 - k_2\eta_2 = 0$, there must have rank($D$) = 2. We can get rank($Z$) = 3 by a similar way. Additionally, as $\boldsymbol{\zeta}^T$ is the normalized vector of the 3rd row of Z^{-1} and $Z^{-1}Z = I$, we have $\boldsymbol{\zeta}^T Z = [0, 0, \boldsymbol{\zeta}^T\boldsymbol{r}_3]$, i.e., $\boldsymbol{\zeta}^T(\boldsymbol{r}_1 - \eta_1\boldsymbol{r}_3) = 0$, $\boldsymbol{\zeta}^T(\boldsymbol{r}_2 - \eta_2\boldsymbol{r}_3) = 0$, which implies $\boldsymbol{\zeta}^T D = \mathbf{0}$ and $D^T\boldsymbol{\zeta} = \mathbf{0}$. ■

The hybrid control force F_{c} is given by

$$\begin{aligned} F_{\mathrm{c}} = &-\Lambda\dot{J}(\boldsymbol{q})\dot{\boldsymbol{q}} - \Lambda JM^{-1}\boldsymbol{\tau}_{\mathrm{e}} - (K_{\mathrm{v}} + \Omega(\boldsymbol{q}, \dot{\boldsymbol{q}}))\dot{\boldsymbol{x}} \\ &- k_{\mathrm{f}}\boldsymbol{\zeta}\boldsymbol{\zeta}^T\tilde{F}_{\mathrm{e}} - DK_{\mathrm{s}}\tilde{\boldsymbol{p}} - \bar{D}^+\bar{D}^T K_{\mathrm{I}}\dot{\boldsymbol{x}}, \end{aligned} \tag{13}$$

with $\bar{D} := [\boldsymbol{d}_1, \boldsymbol{d}_2] \in \mathbb{R}^{3\times2}$ being a full-rank submatrix of D, $\bar{D}^+ := \bar{D}(\bar{D}^T\bar{D})^{-1} \in \mathbb{R}^{3\times2}$, and $\Omega(\boldsymbol{q}, \dot{\boldsymbol{q}}) := -\Lambda JM^{-1}\dot{J}^T\Lambda + \Lambda JM^{-1}CM^{-1}J\Lambda \in \mathbb{R}^{3\times3}$, in which $K_{\mathrm{s}} \in \mathbb{R}^{3\times3}$, $K_{\mathrm{I}} \in \mathbb{R}^{3\times3}$, $K_{\mathrm{v}} \in \mathbb{R}^{3\times3}$ and $k_{\mathrm{f}} \in \mathbb{R}$ are positive-definite control gains, and Ω satisfies the skew-symmetry of $\dot{\Lambda} - 2\Omega$ [20]. Then, substituting (13) into (12) leads to the following closed-loop dynamics in the Cartesian space

$$\Lambda\ddot{\boldsymbol{x}} + (K_{\mathrm{v}} + \bar{D}^+\bar{D}^T K_{\mathrm{I}} + \Omega)\dot{\boldsymbol{x}} = -k_{\mathrm{f}}\boldsymbol{\zeta}\boldsymbol{\zeta}^T\tilde{F}_{\mathrm{e}} - DK_{\mathrm{s}}\tilde{\boldsymbol{p}}. \tag{14}$$

Note that the 3rd column of D is $\mathbf{0}$, and one has $\boldsymbol{\zeta}^T\bar{D} = 0$ and $\bar{D}^T\bar{D}^+\bar{D}^T = \bar{D}^T$ from *Property* 1.

C. Theoretical Results With Stability Analysis

The following theorem concludes the theoretical results of the proposed HVFC method.

Theorem 1: Consider a redundant robotic system (6) driven by the control law composed of (8), (10) and (13). The closed-loop dynamics has global stability in the sense that:

1) The robot manipulator has a compliance behavior in the nullspace (i.e., the projection space of N);
2) The projected contact force error $\boldsymbol{\zeta}^T\tilde{F}_{\mathrm{e}}$ exponentially converges to 0;
3) The pixel error $\tilde{\boldsymbol{p}}$ asymptotically converges to $\mathbf{0}$ such that the tooltip (i.e. the feature point Q) reaches the desired contact point on the surface.

Proof: 1) Left-multiplying both sides of (9) by N and using the property $NM^{-1}J^T = \mathbf{0}$, one obtains the closed-loop dynamics in the nullspace as follows:

$$N(\ddot{\boldsymbol{q}} - \boldsymbol{\tau}_{\mathrm{n}} - M^{-1}\boldsymbol{\tau}_{\mathrm{e}}) = \mathbf{0}. \tag{15}$$

Substituting (10) into (15) yields

$$N\big(\ddot{\tilde{\boldsymbol{q}}} + M_{\mathrm{d}}^{-1}(B_{\mathrm{d}}\dot{\tilde{\boldsymbol{q}}} + K_{\mathrm{d}}\tilde{\boldsymbol{q}}) - M^{-1}\boldsymbol{\tau}_{\mathrm{e}}\big) = \mathbf{0} \tag{16}$$

which shows the compliance feature in the nullspace. Particularly, if the desired inertia is chosen to be the same as the robot inertia, i.e., $M_{\mathrm{d}} = M$, one has

$$NM^{-1}(M\ddot{\tilde{\boldsymbol{q}}} + (B_{\mathrm{d}}\dot{\tilde{\boldsymbol{q}}} + K_{\mathrm{d}}\tilde{\boldsymbol{q}}) - \boldsymbol{\tau}_{\mathrm{e}}) = \mathbf{0}.$$

As $MN = N^T M$, the above equation can be rewritten to

$$N^T(M\ddot{\tilde{\boldsymbol{q}}} + B_{\mathrm{d}}\dot{\tilde{\boldsymbol{q}}} + K_{\mathrm{d}}\tilde{\boldsymbol{q}} - \boldsymbol{\tau}_{\mathrm{e}}) = \mathbf{0}. \tag{17}$$

Thus, the robot has a compliance behavior as $M\ddot{\tilde{\boldsymbol{q}}} + B_{\mathrm{d}}\dot{\tilde{\boldsymbol{q}}} + K_{\mathrm{d}}\tilde{\boldsymbol{q}} - \boldsymbol{\tau}_{\mathrm{e}} = 0$ with the user-specified desired damping B_{d} and desired stiffness K_{d} in nullspace.

2) Left-multiplying both sides of (14) by $\boldsymbol{\zeta}^T$ and using the properties $\boldsymbol{\zeta}^T\boldsymbol{\zeta} = 1$, $\boldsymbol{\zeta}^T D = 0$ and $\boldsymbol{\zeta}^T\bar{D} = 0$ yields

$$\boldsymbol{\zeta}^T\big(\Lambda\ddot{\boldsymbol{x}} + (K_{\mathrm{v}} + \Omega)\dot{\boldsymbol{x}} + k_{\mathrm{f}}\tilde{F}_{\mathrm{e}}\big) = 0. \tag{18}$$

Hence, one obtains the subspace closed-loop dynamics

$$\Lambda\ddot{\boldsymbol{x}} + (K_{\mathrm{v}} + \Omega)\dot{\boldsymbol{x}} = -k_{\mathrm{f}}\tilde{F}_{\mathrm{e}}. \tag{19}$$

The contact model of a rigid surface can be expressed by

$$F_{\mathrm{e}}(t) = K_{\mathrm{o}}(\boldsymbol{x}(t) - \boldsymbol{x}_{\mathrm{o}})$$

where $K_{\mathrm{o}} \in \mathbb{R}^{3\times3}$ is a positive-definite stiffness matrix, and $\boldsymbol{x}_{\mathrm{o}} \in \mathbb{R}^3$ is a constant equilibrium position of the contact point. Thus, for a constant F_{d}, one has $\dot{\tilde{F}}_{\mathrm{e}}(t) = \dot{F}_{\mathrm{e}}(t) = K_{\mathrm{o}}\dot{\boldsymbol{x}}$. Select a Lyapunov candidate function

$$V_{\mathrm{f}} = \dot{\boldsymbol{x}}^T\Lambda\dot{\boldsymbol{x}} + k_{\mathrm{f}}\tilde{F}_{\mathrm{e}}^T K_{\mathrm{o}}^{-1}\tilde{F}_{\mathrm{e}}.$$

Taking the time derivation of V_f leads to

$$\dot{V}_\mathrm{f} = 2\dot{\boldsymbol{x}}^T\Lambda\ddot{\boldsymbol{x}} + \dot{\boldsymbol{x}}^T\dot{\Lambda}\dot{\boldsymbol{x}} + 2k_\mathrm{f}\tilde{F}_\mathrm{e}^T K_\mathrm{o}^{-1}\dot{\tilde{F}}_\mathrm{e}.$$

Applying the above equation, (19) and the skew-symmetry of $\dot{\Lambda}-2\Omega$, one gets $\dot{V}_\mathrm{f} = -2\dot{\boldsymbol{x}}^T K_\mathrm{v}\dot{\boldsymbol{x}} \leq 0$. From the Invariant Set Theorem [21], $\dot{\boldsymbol{x}}$ eventually reaches an invariant set $\mathcal{M}_1 := \{\dot{\boldsymbol{x}}|\dot{V}_\mathrm{f} \equiv 0\}$ with $\dot{\boldsymbol{x}} \equiv 0$, which implies by (19) that $\ddot{\boldsymbol{x}} \equiv 0$ and $\tilde{F}_\mathrm{e} \equiv \mathbf{0}$ in the projection space of $\boldsymbol{\zeta}^T$. Therefore, one obtains the convergence of $\boldsymbol{\zeta}^T\tilde{F}_\mathrm{e} \to 0$ exponentially.

3) Left-multiplying (14) by $\bar{D}^T$ and applying the properties $\bar{D}^T\boldsymbol{\zeta} = \mathbf{0}$ and $\bar{D}^T\bar{D}^+\bar{D}^T = \bar{D}^T$ yields

$$\bar{D}^T\left(\Lambda\ddot{x} + (K_\mathrm{v} + K_\mathrm{I} + \Omega)\dot{\boldsymbol{x}} + DK_\mathrm{s}\tilde{\boldsymbol{p}}\right) = \mathbf{0}.$$

Thus, one gets another subspace closed-loop dynamics

$$\Lambda\ddot{x} + (K_\mathrm{v} + K_\mathrm{I} + \Omega)\dot{\boldsymbol{x}} = -DK_\mathrm{s}\tilde{\boldsymbol{p}}. \tag{20}$$

Select a Lyapunov candidate function

$$V = \frac{1}{2}\dot{\boldsymbol{x}}^T\Lambda\dot{\boldsymbol{x}} + \frac{1}{2}z\tilde{\boldsymbol{p}}^T K_\mathrm{s}\tilde{\boldsymbol{p}}.$$

Calculating $\dot{V}$ and using $\dot{\Lambda} - 2\Omega = \mathbf{0}$ yield

$$\begin{aligned}\dot{V} &= \dot{\boldsymbol{x}}^T\Lambda\ddot{\boldsymbol{x}} + \frac{1}{2}\dot{\boldsymbol{x}}^T\dot{\Lambda}\dot{\boldsymbol{x}} + z\tilde{\boldsymbol{p}}^T K_\mathrm{s}\dot{\tilde{\boldsymbol{p}}} + \frac{1}{2}\dot{z}\tilde{\boldsymbol{p}}^T K_\mathrm{s}\tilde{\boldsymbol{p}} \\ &= z\tilde{\boldsymbol{p}}^T K_\mathrm{s}\dot{\tilde{\boldsymbol{p}}} + \frac{1}{2}\dot{z}\tilde{\boldsymbol{p}}^T K_\mathrm{s}\tilde{\boldsymbol{p}} - \dot{\boldsymbol{x}}^T(K_\mathrm{v} + K_\mathrm{I})\dot{\boldsymbol{x}} - \dot{\boldsymbol{x}}^T DK_\mathrm{s}\tilde{\boldsymbol{p}}.\end{aligned}$$

Applying (4) and (5) results in

$$\begin{aligned}z\tilde{\boldsymbol{p}}^T K_\mathrm{s}\dot{\tilde{\boldsymbol{p}}} + \frac{1}{2}\dot{z}\tilde{\boldsymbol{p}}^T K_\mathrm{s}\tilde{\boldsymbol{p}} &= \dot{\boldsymbol{x}}^T A^T K_\mathrm{s}\tilde{\boldsymbol{p}} + \frac{1}{2}\dot{\boldsymbol{x}}^T\boldsymbol{r}_3\tilde{\boldsymbol{p}}^T K_\mathrm{s}\tilde{\boldsymbol{p}} \\ &= \dot{\boldsymbol{x}}^T(A^T + \frac{1}{2}\boldsymbol{r}_3\tilde{\boldsymbol{p}})K_\mathrm{s}\tilde{\boldsymbol{p}} = \dot{\boldsymbol{x}}^T DK_\mathrm{s}\tilde{\boldsymbol{p}}.\end{aligned}$$

Combining the above two results leads to

$$\dot{V} = -\dot{\boldsymbol{x}}^T(K_\mathrm{v} + K_\mathrm{I})\dot{\boldsymbol{x}} \leq 0.$$

Therefore, $\dot{\boldsymbol{x}}$ ultimately converges to a set $\mathcal{M}_2 := \{\dot{\boldsymbol{x}}|\dot{V} \equiv 0\}$ with $\dot{\boldsymbol{x}} \equiv 0$ from the Invariant Set Theorem [21], which in turn implies $DK_\mathrm{s}\tilde{\boldsymbol{p}} = 0$ from (14). As $\mathrm{rank}(R) = 3$, one has $\mathrm{rank}(D) = \mathrm{rank}(\bar{D}) = 2$ from *Property* 1. Hence, one gets $\tilde{\boldsymbol{p}} = 0$, as $\mathrm{rank}(K_\mathrm{s}) = 3$ and the available dimension of $\tilde{\boldsymbol{p}}$ is 2 excluding the 3rd element with a constant value of 0. ■

Remark 1: In the hybrid control force F_c (13), K_s and k_f are the gains of the pixel error $\tilde{\boldsymbol{p}}$ and the projected force error $\boldsymbol{\zeta}^T\tilde{F}_\mathrm{e}$, respectively. The dynamics in (19) and (20) indicate that K_v is the damping for both vision and force control, while K_I is only used to adjust the damping for vision control.

Remark 2: If $F_\mathrm{d} = f_\mathrm{d}F_\mathrm{e}/\|F_\mathrm{e}\|$ with $f_\mathrm{d} \in \mathbb{R}^+$ being the desired value along the contact force F_e and $\boldsymbol{\zeta}^T\tilde{F}_\mathrm{e} = 0$, one has $(f - f_d)\boldsymbol{\zeta}^T F_\mathrm{e}/\|F_\mathrm{e}\| = 0$, which implies $f - f_d = 0$ when F_e is not in the direction of $\boldsymbol{\zeta}$. Since the normal of a friction-free surface can be denoted by $\boldsymbol{n} = F_\mathrm{e}/\|F_\mathrm{e}\|$, the proposed HVFC method can control the contact force F_e along the surface normal by setting $F_\mathrm{d} = f_\mathrm{d}F_\mathrm{e}/\|F_\mathrm{e}\|$.

IV. Experimental Validation

This section verifies the proposed approach on a seven-DoF redundant collaborative robot named Franka Emika Panda. The experimental setup is shown in Fig. 3, where an ATI Gamma force/torque sensor is installed on the robot end-effector to measure the contact force F_e, torque sensors in each actuator are used to measure the external torque $\boldsymbol{\tau}_\mathrm{e}$, a gripper is mounted on the F/T sensor, a red rectangle marker acting as a feature point Q is attached to its tip, and a monocular ETH camera named RealSense D435i (from Intel Inc.) with 30 frames per second is fixed towards the robot to guarantee that Q is in the view of the camera. The control law (8) with (10) and (13) is implemented on a personal computer with the Robot Operating System and the Ubuntu System. The image feature is extracted

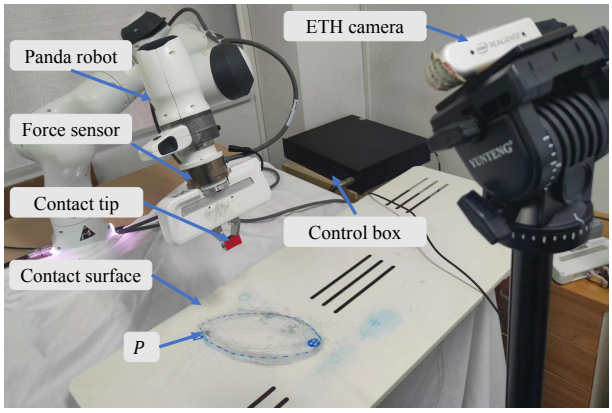

Fig. 3. An experimental setup, where a red rectangle marker is used for position control, and P denotes a contact point on the surface.

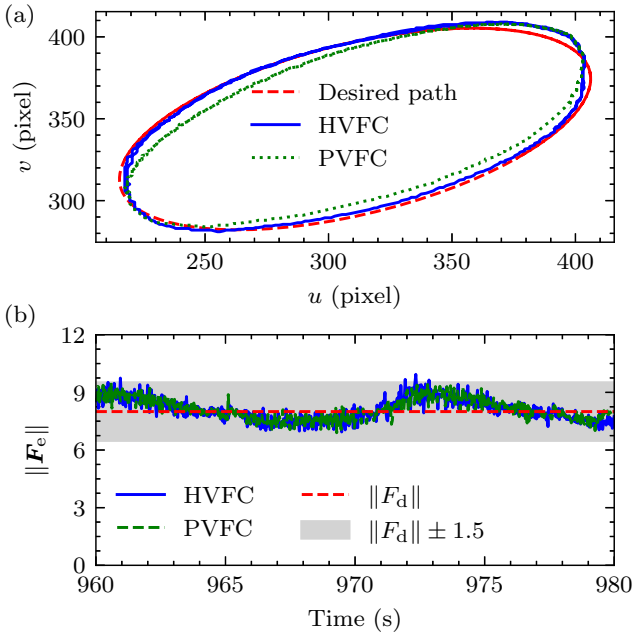

Fig. 4. Experimental results of Case 1. (a) The pixel path $\boldsymbol{p}$ of the tooltip Q on the image plane. (b) The norm of the contact force F_e. Note that we set the desired force $F_\mathrm{d} = f_\mathrm{d}\frac{F_\mathrm{e}}{\|F_\mathrm{e}\|}$ ($f_\mathrm{d} = 8$) as discussed in *Remark* 2.

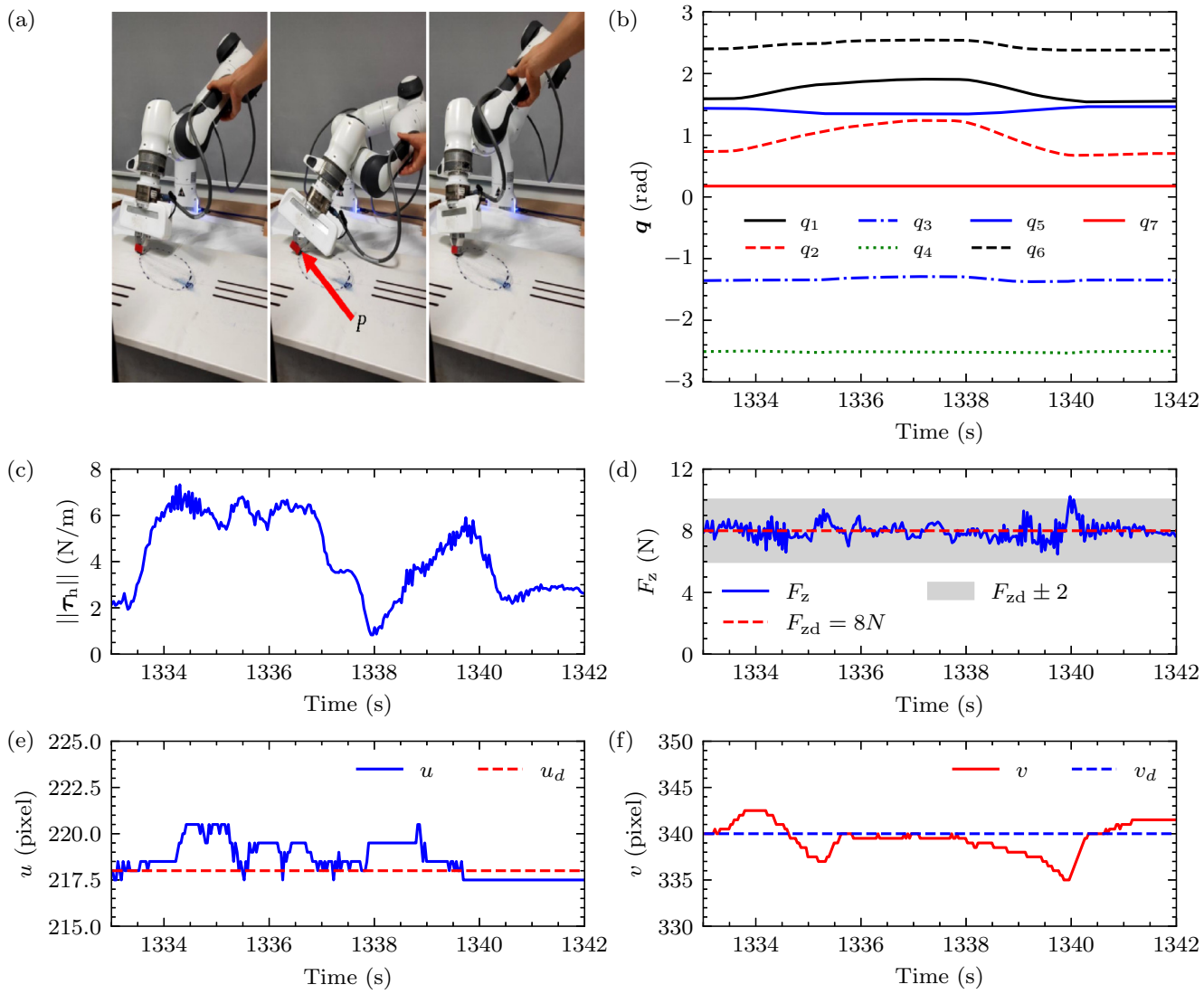

Fig. 5. Experimental results of Case 2. (a) Snapshots of the robot configurations before, during, and after interaction with the human operator. (b) The joint position $\boldsymbol{q}$. (c) The interaction torque $\boldsymbol{\tau}_{\rm h}$. (d) The contact force F_z at the z-axis. (e) The pixel position u at the u-axis. (f) The pixel position v at the v-axis.

by color and shape using OpenCV.

The initial joint configuration is $\boldsymbol{q}(0) = [105,\ 35,\ -95,\ -130,\ 80,\ 140,\ 10]^T$ degrees. Unless otherwise specified, the control parameters in (13) are set as $K_{\rm s} = 0.00012I$, $K_{\rm v} = 10I$, $K_{\rm I} = 34I$, and $k_{\rm f} = 1$. The desired impedance parameters in (8) are set as $M_{\rm d} = M$, $B_{\rm d} = \text{diag}(8, 8, 8, 8, 8, 5, 5)$ and $K_{\rm d} = \text{diag}(4, 4, 4, 4, 2, 2, 2)$. Two experimental cases are considered to validate hybrid control and nullspace compliance, respectively, where in Case 1, the proposed HVFC is compared to a parallel vision-force control (PVFC) method with a parallel scheme in [9] and the control law (8) with (10) and

$$F_{\rm c} = -\Lambda\dot{J}(\boldsymbol{q})\dot{\boldsymbol{q}} - \Lambda JM^{-1}\boldsymbol{\tau}_{\rm e} - (K_{\rm v} + \Omega(\boldsymbol{q}, \dot{\boldsymbol{q}}))\dot{\boldsymbol{x}} - k_{\rm f}\tilde{F}_{\rm e} - DK_{\rm s}\tilde{\boldsymbol{p}} + \bar{D}^{+}\bar{D}^{T}K_{\rm I}\dot{\boldsymbol{x}}.$$

The proposed HVFC has a framework that can decouple the force and vision subspaces, while the PVFC does not control the force in the orthogonal subspace of the vision task space. The parameters of the two controllers are set the same for fair comparisons. Unlike the HVFC, the force control of the PVFC is not achieved in the individual projection space.

Case 1: A slow tracking task is designed as a repeating polishing or wiping task on a planar surface with an unknown slope (i.e., the unknown surface normal). The desired trajectory $\boldsymbol{p}_{\rm d} := [u_d, v_d, 1]^T$ is an ellipse that can be expressed by

$$\boldsymbol{a} = (\boldsymbol{p}_1 - \boldsymbol{p}_2)/2,\ \boldsymbol{b} = (\boldsymbol{p}_1 + \boldsymbol{p}_2)/2,$$
$$u = b_1 + a_1\cos(0.5t) + \frac{50a_2}{\|\boldsymbol{a}\|}\sin(0.5t),$$
$$v = b_2 + a_2\cos(0.5t) - \frac{50a_1}{\|\boldsymbol{a}\|}\sin(0.5t)$$

with a_i and b_i being the ith element of $\boldsymbol{a}$ and $\boldsymbol{b}$, respectively, where $\boldsymbol{p}_1$ and $\boldsymbol{p}_2$ are two-pixel positions that are manually selected on the image plane. The desired contact force is set to $F_{\rm d} = 8\frac{F_{\rm e}}{\|F_{\rm e}\|}$ N. Although high-accuracy tracking is not shown by both methods as they are designed for position regulation, the path of the tooltip Q by the proposed HVFC is much closer

to the desired path $\boldsymbol{p}_{\mathrm{d}}$ [see Fig. 4(a)], despite of their similar force control performance with a maximum error of 1.5 N between the norms $\|F_{\mathrm{e}}\|$ and $\|F_{\mathrm{d}}\|$ [see Fig. 4(b)].

Case 2: An experiment is designed to show the nullspace compliance of the robot. As the planar surface has a normal close to the z-axis of the world frame $\{B\}$ in this experiment, only the contact force F_{z} along $z-$axis is considered with its desired value $F_{\mathrm{zd}} = 8$ N. The desired pixel position $\boldsymbol{p}_{\mathrm{d}}$ is manually selected to match the pixel position of P. A human operator exerts an interaction tore $\boldsymbol{\tau}_{\mathrm{h}} \in \mathbb{R}^7$ (calculated by $\boldsymbol{\tau}_{\mathrm{h}} = \boldsymbol{\tau}_{\mathrm{e}} - J^T F_{\mathrm{e}}$) on the robot by pulling and dragging the 5th link [see Fig. 5(a)]. Experimental results show that the joint position $\boldsymbol{q}$ varies with $\boldsymbol{\tau}_{\mathrm{h}}$, resulting in a mild interaction torque with $||\boldsymbol{\tau}_{\mathrm{h}}|| < 8$ N/m [see Fig. 5(b)-(c)]. Note that $\boldsymbol{q}$ would not recover after $\boldsymbol{\tau}_{\mathrm{h}} = 0$ due to the small stiffness K_{d} and friction. On the other hand, the pixel positions u and v of Q deviate from their desired values u_{d} and v_{d} within 5 pixels, respectively, and the contact force F_{z} deviates from its desired value F_{dz} within 2 N [see Figs. (c)-(f)], which indicates that the nullspace compliant interaction has tiny influences on the contact task in the Cartesian space.

V. Conclusion

This paper has proposed a unified framework of HVFC and nullspace compliance for redundant robots with contact tasks, where vision feedback from an ETH monocular camera is applied for position control on contact surfaces, and force feedback from a force sensor is utilized for direct contact force control. The proposed method achieves position and force control on the surface without prior geometric knowledge and impedance control in the joint nullspace, which prevents harmful contact forces. Experiments on a seven-DoF redundant robot have validated the above distinctive features. Future work would focus on improving tracking performance and compliant visual control in contact tasks.

References

[1] A. Billard and D. Kragic, "Trends and challenges in robot manipulation," *Sci. Robot.*, vol. 364, no. 6446, Jun. 2019, Art. No. eaat8414.

[2] M. K. Vukobratović and V. Potkonjak, "Dynamics of contact tasks in robotics. part I: General model of robot interacting with environment," *Mech. Mach. Theory*, vol. 34, no. 6, pp. 923–942, Aug. 1999.

[3] C. P. Bechlioulis, Z. Doulgeri, and G. A. Rovithakis, "Neuro-adaptive force/position control with prescribed performance and guaranteed contact maintenance," *IEEE Trans. Neural Netw.*, vol. 21, no. 12, pp. 1857–1868, Oct. 2010.

[4] Y. Karayiannidis, G. A. Rovithakis, and Z. Doulgeri, "Force/position tracking for a robotic manipulator in compliant contact with a surface using neuro-adaptive control," *Automatica*, vol. 43, pp. 1281–1288, Jul. 2007.

[5] J. C. Santos, L. Cuau, P. Poignet, and N. Zemiti, "Decoupled model predictive control for path following on complex surfaces," *IEEE Robot. Autom. Lett.*, vol. 8, no. 4, pp. 2046–2053, Feb. 2023.

[6] Y. Karayiannidis and Z. Doulgeri, "Robot contact tasks in the presence of control target distortions," *Robot. Auton. Syst.*, vol. 58, pp. 596–606, May. 2010.

[7] Z. Doulgeri and Y. Karayiannidis, "Force/position regulation for a robot in compliant contact using adaptive surface slope identification," *IEEE Trans. Autom. Control*, vol. 53, no. 9, pp. 2116–2122, Oct. 2008.

[8] J. Li, Y. Guan, H. Chen, B. Wang, and T. Zhang, "Robotic polishing of unknown-model workpieces with constant normal contact force control," *IEEE/ASME Trans. Mechatron.*, vol. 28, no. 2, pp. 1093–1103, Apr. 2023.

[9] M. Suomalainen, Y. Karayiannidis, and V. Kyrki, "A survey of robot manipulation in contact," *Robot. Auton. Syst.*, vol. 156, Oct. 2022, Art. No.104224.

[10] M. Xu, A. Hu, and H. Wang, "Image-based visual impedance force control for contact aerial manipulation," *IEEE Trans. Autom. Sci. Eng.*, vol. 20, no. 1, pp. 518–527, Jan. 2023.

[11] B. Ahmadi, W.-F. Xie, and E. Zakeri, "Robust cascade vision/force control of industrial robots utilizing continuous integral sliding-mode control method," *IEEE/ASME Trans. Mechatron.*, vol. 27, no. 1, pp. 524–536, Feb. 2021.

[12] E. C. Dean-León, V. Parra-Vega, and A. Espinosa-Romero, "Visual servoing for constrained planar robots subject to complex friction," *IEEE/ASME Trans. Mechatron.*, vol. 11, no. 4, pp. 389–400, Aug. 2006.

[13] A. C. Leite, F. Lizarralde, and L. Hsu, "Hybrid adaptive vision—force control for robot manipulators interacting with unknown surfaces," *Int. J. Robot. Res*, vol. 28, no. 7, pp. 911–926, Jul. 2009.

[14] C. C. Cheah, S. P. Hou, Y. Zhao, and J.-J. E. Slotine, "Adaptive vision and force tracking control for robots with constraint uncertainty," *IEEE/ASME Trans. Mechatron.*, vol. 15, no. 3, pp. 389–399, Aug. 2009.

[15] F. Xu, H. Wang, Z. Liu, W. Chen, and Y. Wang, "Visual servoing pushing control of the soft robot with active pushing force regulation," *Soft Robot.*, vol. 9, no. 4, pp. 690–704, Aug. 2022.

[16] Z. Li, B. Lai, and Y. Pan, "Image-based composite learning robot visual servoing with an uncalibrated eye-to-hand camera," *IEEE/ASME Trans. Mechatron.*, vol. 29, no. 4, pp. 2499 – 2509, Aug. 2024.

[17] A. D. Luca and R. Mattone, "Sensorless robot collision detection and hybrid force/motion control," in *Proc. IEEE Int. Conf. Robot. Autom.*, Barcelona, Spain, 2005, pp. 999–1004.

[18] A. Dietrich, C. Ott, and A. O. Albu-Schäffer, "An overview of null space projections for redundant, torque-controlled robots," *Int. J. Robot. Res*, vol. 34, no. 11, pp. 1385 – 1400, Mar. 2015.

[19] Z. Li, W. Li, and Y. Pan, "Composite learning image-based visual servoing of redundant robots with nullspace compliance," *IEEE Control Syst. Lett.*, vol. 8, pp. 315–320, Jan. 2024.

[20] H. Sadeghian, L. Villani, M. Keshmiri, and B. Siciliano, "Task-space control of robot manipulators with null-space compliance," *IEEE Trans. Robot.*, vol. 30, no. 2, pp. 493–506, Apr. 2014.

[21] I. Barkana, "Defending the beauty of the invariance principle," *Int. J. Control*, vol. 87, no. 1, pp. 186–206, 2014.